Elsevier Editorial System(tm) for Earth and Planetary Science Letters
Manuscript Draft

Manuscript Number: EPSL-D-16-00663R2

Title: Formation of Obsidian Pyroclasts by Sintering of Ash Particles in the Volcanic Conduit

Article Type: Letters

Keywords: obsidian; explosive eruption; volatiles; Mono Craters; degassing; vesicle

Corresponding Author: Dr. James E. Gardner,

Corresponding Author's Institution: The University of Texas at Austin

First Author: James E. Gardner

Order of Authors: James E. Gardner; Edward W Llewellin; James M Watkins; Kenneth S Befus

Abstract: The ranges in intensity and style of volcanic eruptions, from highly explosive Plinian eruptions to quiescent lava extrusions, depend on the style and efficiency of gas loss from ascending magma. Obsidian pyroclasts - small, glassy pieces of quenched magma found in some volcanic tephra beds - may preserve valuable information about magma degassing in their vesicle textures and volatile contents. Accurate interpretation of their textures and volatiles, however, requires understanding the mechanism of formation of the pyroclasts. Obsidian pyroclasts from the ca. 1325-1350 C.E. North Mono eruption of Mono Craters (CA, USA) were analyzed and found to have H_2O and CO_2 contents indicating that they were formed at pressures in the approximate range 3-40 MPa. Many also contain domains with differing vesicle textures, separated by boundaries containing xenocrystic material, indicating that they are composed of smaller fragments that have sutured together. More than half of the pyroclasts analyzed contained small (~10 µm), highly distorted vesicles, with multi-cuspate morphology, interpreted as the remnants of interstitial gas trapped amongst sintered fragments of melt/glass. Rounded vesicles are also common and are interpreted to result from surface tension-driven relaxation of the distorted vesicles. Calculated timescales of sintering and relaxation are consistent with timescales for pyroclast formation indicated by H_2O re-equilibration within the heterogeneous pyroclasts. This sintering model for the origin of obsidian pyroclasts is further supported by the observation that spherical vesicles are found mainly in H_2O-rich pyroclasts, and distorted vesicles mainly in H_2O-poor pyroclasts. We conclude that obsidian pyroclasts generated during the North Mono eruption were formed by cycles of fragmentation, sintering/suturing, and relaxation, over a very wide range of depths within the conduit; we find no evidence to support pumice (foam) collapse as the formation mechanism. Similar textures, and the occurrence of xenolithic material, in obsidian pyroclasts in other eruptions suggest that sintering may be generally responsible for the origin of obsidian pyroclasts. Our conceptual model indicates that volatile contents in obsidian pyroclasts reflect both degassing of bubbly magma and the composition of gas trapped between sintering particles.

Highlights

- Vesicles and volatile contents were measured in Mono Craters obsidian pyroclasts
- Vesicle textures argue for formation of obsidian pyroclasts through ash sintering
- Obsidians made of domains that underwent different degassing and shear histories
- Obsidian pyroclasts formed by cycles of fragmentation, sintering, and relaxation
- No evidence found for obsidian pyroclasts formation by pumice (foam) collapse

Formation of Obsidian Pyroclasts by Sintering of Ash Particles in the Volcanic Conduit

James E. Gardner[a,*], Edward W. Llewellin[b], James M. Watkins[c], and Kenneth S. Befus[d]

[a]*Department of Geological Sciences, Jackson School of Geosciences, The University of Texas at Austin, Austin, TX, 78712-0254, U.S.A.*
[b]*Department of Earth Sciences, Durham University, Durham, DH1 3LE, U.K.*
[c]*Department of Earth Sciences, University of Oregon, Eugene, OR, 97403-1272, U.S.A.*
[d]*Department of Geosciences, Baylor University, Waco, TX, 76798, U.S.A.*

[*]Corresponding author. Fax: +1 512 471 9425
E-mail address: gardner@mail.utexas.edu (J.E. Gardner)

ABSTRACT

The ranges in intensity and style of volcanic eruptions, from highly explosive Plinian eruptions to quiescent lava extrusions, depend on the style and efficiency of gas loss from ascending magma. Obsidian pyroclasts – small, glassy pieces of quenched magma found in some volcanic tephra beds – may preserve valuable information about magma degassing in their vesicle textures and volatile contents. Accurate interpretation of their textures and volatiles, however, requires understanding the mechanism of formation of the pyroclasts. Obsidian pyroclasts from the ca. 1325–1350 C.E. North Mono eruption of Mono Craters (CA, USA) were analyzed and found to have H_2O and CO_2 contents indicating that they were formed at pressures in the approximate range 3–40 MPa. Many also contain domains with differing vesicle textures, separated by boundaries containing xenocrystic material, indicating that they are composed of smaller fragments that have sutured together. More than half of the pyroclasts analyzed contained small (~10 μm), highly distorted vesicles, with multi-cuspate morphology, interpreted as the remnants of interstitial gas trapped amongst sintered fragments of melt/glass. Rounded vesicles are also common and are interpreted to result from surface tension-driven relaxation of the distorted vesicles. Calculated timescales of sintering and relaxation are consistent with timescales for pyroclast formation indicated by H_2O re-equilibration within the heterogeneous pyroclasts. This sintering model for the origin of obsidian pyroclasts is further supported by the observation that spherical vesicles are found mainly in H_2O–rich pyroclasts, and distorted vesicles mainly in H_2O–poor pyroclasts. We conclude that obsidian pyroclasts generated during the North Mono eruption were formed by cycles of fragmentation, sintering/suturing, and relaxation, over a very wide range of depths within the conduit; we find no evidence to support pumice (foam) collapse as the formation mechanism. Similar textures, and the occurrence of xenolithic material, in obsidian pyroclasts in other eruptions suggest that sintering may be generally responsible for the origin of obsidian pyroclasts. Our conceptual model indicates that volatile contents in obsidian pyroclasts reflect both degassing of bubbly magma and the composition of gas trapped between sintering particles.

Keywords:

obsidian

explosive eruption

volatiles

Mono Craters

degassing

vesicle

1. Introduction

The style of silicic volcanic eruptions depends on the behavior of gas that exsolves from magma during ascent (Eichelberger et al., 1986; Jaupart and Allegre, 1991; Gonnermann and Manga, 2003). In the current paradigm, if the gas remains trapped in the bubbly magma (closed–system degassing), then the magma will eventually fragment, driving explosive activity. If, instead, the magma becomes permeable, allowing the gas to escape (open–system degassing), then the magma does not fragment, but collapses to a bubble-poor liquid and effuses as lava (Eichelberger et al., 1986).

Evidence for magma degassing (exsolution of magmatic volatiles from the melt) and outgassing (loss of exsolved gas from the magma) is preserved in obsidian pyroclasts – glassy pieces of quenched magma found in some volcanic tephras (e.g., Eichelberger and Westrich, 1981; Taylor et al., 1983; Newman et al., 1988; Rust et al., 2004; Barnes et al., 2014). Variations in concentrations and isotopic compositions of volatiles among obsidian pyroclasts often appear to follow trends expected from closed–system degassing (Taylor et al., 1983; Newman et al., 1988; Barnes et al., 2014). This presents a problem because obsidian pyroclasts are vesicle-poor, yet closed-system degassing implies that gas bubbles remain within the packet of magma in which they form. Various models have been proposed to explain this apparent conundrum, hypothesizing that the closed–system–like volatile signatures arise from disequilibrium bubble growth (Gonnerman and Manga, 2005) or from buffering the magma by CO_2–rich gas that streams through brecciated magma (Rust et al., 2004). Rust et al. (2004) also propose that some obsidian pyroclasts form by 'annealing' of glass/melt fragments at the conduit margin, challenging the foam-collapse model for their origin (Eichelberger et al., 1986).

In this study, we investigate the origin and evolution of vesicles in obsidian pyroclasts from the most recent eruption of Mono Craters (Sieh and Bursik, 1986) by comparing vesicle textures to the preserved volatile contents. Based on our observations we go further than Rust et al. (2004) and argue that most, if not all, of the obsidian pyroclasts originate from sintering of small glass/melt fragments in the conduit (sintering is used in preference to annealing, following Wadsworth et al., 2014, 2016). Volatile contents in obsidian pyroclasts thus reflect the composition of gas trapped between sintered ash fragments, rather than preserve degassing trends.

2. Methods

Obsidian pyroclasts were collected from the North Mono tephra bed, dated to the interval 1325–1350 C.E. (Sieh and Bursik, 1986; Bursik, 1993). The eruption began with a series of sub-plinian explosions that spread a thick blanket of tephra to the north and east of Mono Craters (Fig. 1). The eruption shifted to producing pyroclastic surges and flows, and ended by extruding at least five lava domes and flows (coulees) (Sieh and Bursik, 1986). As many as 10 vents were active, and their alignment, plus the extrusion of separate lavas, suggest that the eruption was fed from one or more dikes (Sieh and Bursik, 1986).

Samples were collected from two pits dug into the North Mono tephra (Fig. 1). The stratigraphy is the same between pits, and can be matched with that described in Sieh and

Bursik (1986); our layers P2, P4, and P6 match their Beds 2, 4, and 6. The relatively lithic- and obsidian-rich nature of P10 suggests it is Bed 7, but it could also be a coarse layer in their Gray Glassy Beds. Bursik (1993) found that Beds 1–6 have ~60–90% pumice and ~1–20% obsidian pyroclasts, with different types of lithics making up the difference. Their Bed 7 contains ~40% obsidian pyroclasts and subordinate amounts of pumice and lithics. Although we did not sieve our tephra layers, those proportions are consistent with our observations.

A total of 81 obsidian pyroclasts collected from four tephra layers were analyzed in this study (Fig. 1). All methods are discussed in the Supplemental text; results are presented in Supplemental Tables A.1 to A.7. Vesicle textures were analyzed in 80 of the obsidian pyroclasts. Volatile contents of 54 were measured in this study; volatile contents of the other 27 were reported in Barnes et al. (2014). Together, the measured volatile contents span the entire range of values reported by Newman et al. (1988) and Rust et al. (2004). Vesicularities of 221 pumice and 23 obsidian pyroclasts were also measured.

3. Results

3.1. Vesicularities and Vesicle Textures of Pumice Clasts

Pumice clasts are gray to white in color, and have vesicularities that range from 20 to 78 vol.% (Fig. 2). The distribution of vesicularity in each layer is unimodal, with means between 56 and 68 vol.%. We scanned 14 pumice clasts by High-Resolution X-ray

Computed Tomography (HRXCT), and classify them as "highly" vesicular (71–74 vol.%), "moderately" vesicular (52–60 vol.%), and "slightly" vesicular (29–44 vol.%).

Highly vesicular pumice clasts have elongated (stretched) vesicles, which range widely in size (Fig. 3a). There are planes of kinked (sheared) vesicles that span parts of each clast. Vesicles in most of the moderately vesicular pumice clasts are generally smaller and more uniform in size than those in the highly vesicular samples (Fig. 3b). One moderately vesicular sample, however, has a micro-vesicular interior (Fig. 3c). The boundary between its outer and inner portions is gradational, and so it is not a dense core mantled by more vesicular material. Slightly vesicular pumice lapilli are more diverse texturally. Some are micro-vesicular, like the dense core of the moderately vesicular pumice clast (Fig. 3d). Others consist of highly stretched vesicles, like denser versions of more vesicular clasts (Fig. 3e). Another of these (38 vol.%) is in fact an amalgamation of small vesicular fragments sutured together by crystal-rich ash that contains rock fragments (Fig. 3f). This was the only such pumice found.

3.2. Volatile and Crystal Contents of Obsidian Pyroclasts

Dissolved concentrations of H_2O and CO_2 in the obsidian pyroclasts range from 0.49 to 2.24 wt.% and from 2 to 45 ppm, respectively (Table A.1). These values overlap those reported by Newman et al. (1988) and Rust et al. (2004). Watkins et al. (in press) mapped H_2O and CO_2 across eight of the obsidian clasts and found that concentrations within each varies, on average, by ±0.3 wt.% H_2O and ±10 ppm CO_2. These internal variations are typically small compared to the spread between samples (Fig. 4; note that vesicle shapes reported in that figure are discussed later). A wide range in volatile contents is found in each tephra layer, but overall there is a general decrease in H_2O and CO_2 contents with increasing stratigraphic height, a trend also found by Newman et al. (1988) and Rust et al. (2004).

All obsidian pyroclasts contain ≤1 vol.% microphenocrysts and microlites (as distinct from xenocrysts described in Section 3.5). Microphenocrysts include quartz, plagioclase, alkali feldspar, biotite, and hornblende. Microlites (up to a few 10's of microns in size) consist of acicular pyroxene, tabular to skeletal feldspar, and tiny Fe–Ti oxides. Fe–Ti oxide microlites can be disseminated throughout a clast or concentrated in bands. Some clasts contain both concentrated bands and disseminated oxides. Most (60 out of 81) obsidian pyroclasts contain pyroxene and/or feldspar microlites, and all but a few have Fe–Ti oxides. Neither microlite abundance nor type correlates with volatile content in our sample set; however, data in figure 14a of Rust and Cashman (2007) suggest that obsidian pyroclasts in the basal layer of the tephra section – which was not sampled in our study – tend to be richer in microlites, and have lower-than-typical H_2O contents.

3.3. Vesicle Textures and Abundances in Obsidian Pyroclasts

All but three obsidian pyroclasts contain vesicles (Table A.1). Vesicularities measured in a subset (23 out of 81) of samples range from 0.02 to 8.4 vol.%, although the majority have <1 vol.% (Fig. 2). No obsidian pyroclast appears more vesicular, and those measured cover the range of vesicle textures (described below); the range of 0.02–8.4 vol.% is thus representative of the population. Vesicles are distributed heterogeneously, typically in bands or clusters, rather than being dispersed homogeneously. Vesicle number density (N_V) spans many orders of magnitude (Table A.1). More than half of those measured have $N_V > 10^{6.8}$ vesicles cm^{-3}, with the highest being $10^{8.1}$ cm^{-3}. The lowest measured N_V is $10^{4.3}$ cm^{-3}, although three obsidians lack vesicles entirely.

A total of 6958 vesicles were measured in 57 obsidian pyroclasts optically and using HRXCT (Tables A.2 to A.7). Vesicles vary widely in shape, but most can be classified in 5 categories, which we call spherical (Fig. 5a, b), rounded ellipsoid (Fig. 5c), sharp-tipped ellipsoid (Fig. 5d), distorted (Fig. 6a–c), and stretched–distorted (Fig. 6d–f). While we group data together based on shape and describe the five classes separately, many pyroclasts contain more than one type of vesicle (Table A.1).

Spherical – Spherical vesicles are equant in shape (the three axis lengths are within 10% of each other) and have smooth, concave surfaces (Fig. 5a). They occur mainly in H_2O–rich obsidian pyroclasts (Fig. 4). They are ~1 to 120 µm in size (Table A.3), with a median of 10 µm, and tend to be larger at higher H_2O contents. Overall, their N_V ranges between $10^{4.3}$–$10^{8.0}$ cm^{-3} (Table A.1), and occur both in isolation and in clusters (Fig. 5b).

Rounded ellipsoid – Ellipsoidal vesicles have smooth, concave surfaces, like spherical ones, but are elongated by >10% in one direction (Fig. 5c, d). They can be divided into two sub-categories, based on the curvature at the end of the long axis. Rounded ellipsoids have dome-shaped ends that are curved slightly more tightly than other parts of the vesicle (Fig. 5c). Sharp-tipped ellipsoids (discussed in the next subsection) come to relatively narrow points with much tighter curvature (Fig. 5d).

Rounded ellipsoid vesicles are found mainly in H_2O–rich obsidian pyroclasts (Fig. 4) and occur in N_V from $10^{4.8}$ to $10^{7.6}$ cm^{-3} (Table A.1). Their long axes range from 4 to

1880 μm, with short axes from ~1 to 300 μm (Table A.4). Intermediate axes are generally closer in length to short axes. Their sizes correlate with H_2O content, and larger vesicles are usually found in smaller N_V. The degree of elongation can be described by a deformation parameter (D), where

$$D = \frac{l_a - l_b}{l_a + l_b} \quad (1)$$

with l_a and l_b being the lengths of the long and short axis (Taylor, 1934; Rust and Manga, 2002). For rounded ellipsoid vesicles, D ranges from ~0.050 (almost spherical) to 0.885 (highly elongated), with larger vesicles tending to be more elongated.

<u>*Sharp-tipped ellipsoid*</u> – Sharp–tipped ellipsoid vesicles (Fig. 5d) are rarer than rounded ones, but occur over a wider range of H_2O contents (Fig. 4) and in N_V values typically <10^5 cm^{-3} (Table A.1). Long axes range from ~4 to 1070 μm; short axes, from ~1 to 270 μm (Table A.5). Their sizes correlate weakly with H_2O content, and their D values range from ~0.050 to 0.863.

<u>*Distorted*</u> – Distorted vesicles are very irregularly shaped, with jagged edges, sharp contortions, convex and concave surfaces, and offshoots (Fig. 6a–c). They are transparent, isotropic, and hollow when exposed, proving they are vesicles. They occur in obsidian pyroclasts across the spectrum of volatile contents, but are more common in those with ≤1.5 wt.% H_2O (Fig. 4). They tend to be numerous, with N_V values of $10^{5.3–7.6}$ cm^{-3} (Table A.1), and most commonly occur in bands that cross the length of an obsidian pyroclast (Fig. 6a) or in isolated clusters (Fig. 6c). The bands often link together in three dimensions and surround regions of less vesicular glass. Characterizing their shapes is

difficult because of their irregularity. Roughly, their median size is 4 μm × 10 μm (Table A.6), but can reach ~120 μm in length, and are usually bladed in shape. Larger ones tend to be wider and have smoother surfaces.

Stretched-distorted – "Stretched-distorted" vesicles look similar to distorted ones, except they are significantly elongated in one direction (Fig. 6d, e). Usually, they are stretched in a common direction (Fig. 6d), and are deformed along planes in some instances (Fig. 6f). Like distorted vesicles, these vesicles occur mainly in H_2O–poorer pyroclasts (Fig. 4) and tend to be numerous, mostly N_V >10^7 cm^{-3} (Table A.1). The longest dimension ranges from ~2–222 μm (median = 11 μm), while their shortest dimension is <1–32 μm (median = 2 μm) (Table A.7). There is no correlation between their size and volatile contents.

3.4. Vesicle associations and assemblages

Approximately 40% of obsidian pyroclasts contain more than one type of vesicle (Table A.1). Spherical vesicles occur most commonly with rounded ellipsoid vesicles (e.g., Fig 5c). Stretched–distorted vesicles occur most commonly with sharp–tipped ellipsoid vesicles, but distorted vesicles occur most commonly with stretched–distorted vesicles. On the other hand, rounded ellipsoid vesicles never occur with distorted or stretched–distorted vesicles, and stretched–distorted vesicles never occur with spherical vesicles.

Some obsidian pyroclasts consist of domains with different vesicle textures (Fig. 7). Some domains differ in abundances of the same vesicle type, others by degrees of vesicle elongation, and some differ substantially by the alignment of elongated vesicles. About 20% of the obsidian pyroclasts have strongly discordant domains. Volatile contents can also differ between domains (e.g., Fig. 8a). It thus appears that a significant fraction of obsidian pyroclasts are composed of smaller fragments that have welded together.

3.5. Xenocryst Fragments and Abundances

Many obsidian pyroclasts contain distinct bands with numerous pieces of crystals, on order of ~1 to 10 µm in size (Fig. 8). They are identified as crystalline by their relief, birefringence (Fig. 8c), and brightness in reflected light. Their jagged edges suggest that many are broken fragments. The bands can be isolated or grouped together, and often contain large crystals and rock fragments (Fig. 7b). The crystal-rich nature of these bands is in sharp contrast to the nearly holohyaline host rhyolite (Fig. 8c). Bands in four different obsidian pyroclasts were all found to contain quartz, alkali feldspar, plagioclase, biotite, hornblende, and Fe-Ti oxides (typically magnetite); some also contain apatite.

The sharp contrast in crystal content, and the common coexistence with rock fragments and anomalously large crystals, indicate that the bands are xenocrystic, and we identify them as the "xenolithic powder" seen by Rust et al. (2004). The crystal assemblage of these bands matches that in many Mono Craters rhyolitic domes and lavas (Kelleher and Cameron, 1990), and so the bands are not small blebs of mafic magma or excavated carbonate lake sediments. Slightly elevated (by ~10 ppm) CO_2 contents are associated with some bands, but not all. This differs from the association of locally highly elevated CO_2 contents with "xenocrystic dust" in obsidian pyroclasts from

Newberry volcano (Rust and Cashman, 2007). We do not consider these bands to be tuffisite veins, which can occur in rhyolitic lavas and pyroclasts, because those tend to be cracks filled with ashy material derived from the erupting magma (Stasiuk et al., 1996; Gonnerman and Manga, 2003; Tuffen et al., 2003; Noguchi et al., 2008; Castro et al., 2012; Kolzenburg et al., 2012).

Some xenocryst bands cut across entire obsidian pyroclasts; they are usually planar and extend 100’s of microns (and farther) in two directions, but are only a few to 10’s of microns in the third dimension. Their margins are usually sharp (Fig. 8a), but some are diffuse and appear smeared out. Some bands thin and grade into discontinuous trails of crystal fragments (Fig. 8d). Isolated trails of xenocrysts – sometimes only a few 10’s of microns long – are seen in many pyroclasts, including those without distinct bands. Vesicles within xenocryst bands are most commonly distorted or stretched–distorted (Fig. 7b, 8b). The bands can be orientated up to ~45° to vesicles (Fig. 7b). In many cases, the margins that separate vesicular domains within obsidian pyroclasts are xenocryst bands (Fig. 7b). Together, xenocryst bands and discontinuous trails are found in ~68% of the pyroclasts, across the entire spectrum of H_2O and CO_2 contents.

4. Discussion

Obsidian pyroclasts form by viscous deformation, and thus any model for their formation requires consideration of their thermal history. Newman et al. (1988) suggest that obsidian pyroclasts represent the “cool glassy margins” of the volcanic conduit. Furthermore, Rust et al. (2004) propose that the chilled margins may cross the glass transition multiple times during their formation. Consequently, obsidian pyroclasts may experience temperatures from magmatic (T_m) to below the glass transition (T_g). To determine an approximate value for T_m, we analyzed the compositions of 10 pairs of magnetite–ilmenite phenocrysts in four of the Mono Craters rhyolite flows, and found temperatures of 744 to 820°C (Ghiorso and Evans, 2008); for convenience we adopt 800°C as T_m. Viscous deformation ceases below T_g, which is often taken as the temperature at which melt viscosity (η) = 10^{12} Pa s [a value relevant for rhyolite cooling at a rate of order 1 K min^{-1} (Gottsmann et al., 2002)]; we use this definition to set the lower temperature bound of interest. For H_2O contents of 0.49 to 2.2 wt.%, T_g ranges from ~600 to ~465°C (Hess and Dingwell, 1996). The thermal range of interest, therefore, is ~200–335°C, depending on H_2O content.

Watkins et al. (in press) report heterogeneities in H_2O and CO_2 contents within individual obsidian pyroclasts (e.g., Fig. 8a), and used diffusion modeling to show that the observed heterogeneities would be erased in a matter of hours at T_m, regardless of H_2O content. Diffusion slows at lower temperature (Ni and Zhang, 2008) and at T_g, the maximum time allowed by the observed heterogeneities increases by a factor of 10–100 compared with T_m. Watkins et al. (in press) concluded that obsidian pyroclasts are composed of subdomains of melt or sintered ash that were juxtaposed above T_g within a few hours prior to quenching.

4.1. Interpretation of Vesicle Shapes in Obsidian Pyroclasts

We argue that all vesicle textures can be produced by starting with populations of distorted bubbles, followed by variable degrees and timing of shear and relaxation. Relaxation occurs when $T > T_g$ because bubbles tend to become spherical over time under the action of surface tension (σ) (N m^{-1}). The characteristic timescale over which a non-spherical bubble relaxes towards spherical is the relaxation time (λ_b), which is given by

$$\lambda_b = \frac{\eta\, r}{\sigma} \tag{2}$$

where r (m) is the equivalent spherical radius of the bubble (Taylor, 1934; Rust and Manga, 2002; Llewellin and Manga, 2005). If a spherical bubble is deformed by simple shear, pure shear, or a combination of the two, it becomes ellipsoidal and, at steady strain rate ($\dot{\gamma}$) (s^{-1}), the shape, described by D (Equation 1) is a simple function of the capillary number ($Ca = \lambda_b\dot{\gamma}$) (Taylor, 1934; Rust and Manga, 2002). Above a critical Ca (i.e. for high strain rate) ellipsoidal bubbles develop sharp tips. The variation among spherical, rounded ellipsoid, and sharp–tipped ellipsoid vesicles can therefore be explained by varying degrees of shearing, and subsequent relaxation, of initially spherical bubbles.

Highly complex shapes like those of the distorted vesicles cannot be produced by variations in shear and relaxation of spherical bubbles (e.g., Rust and Manga, 2002). Moreover, distorted vesicles are generally not aligned (Fig. 6a), which would be expected if they formed by shearing. On the other hand, stretched–distorted vesicles are typically aligned; we thus infer that they formed by shearing of distorted bubbles. While it is not possible to form distorted vesicles by shear deformation of spherical bubbles, distorted bubbles will tend to relax towards spherical over time (Rust and Manga, 2002). Applying shear at different times during the relaxation of distorted bubbles could lead to either stretched–distorted vesicles (if applied relatively early) or ellipsoid vesicles (if applied relatively late).

4.2. Evidence for a Fragmental Origin for Obsidian Pyroclasts

The occurrence of xenocryst bands and rock fragments in a large majority of obsidian pyroclasts is strong evidence that the obsidians did not form by pumice (foam) collapse (Eichelberger et al., 1986; Westrich and Eichelberger, 1994). This interpretation is supported by the observation that many obsidian pyroclasts are composed of domains that experienced different vesiculation and deformation histories (Figs. 6, 7). In addition, the wide gap in vesicularity between obsidian and pumice (Fig. 2) is hard to reconcile with a foam-collapse origin, which would necessitate that the magma passed through a stage of intermediate vesicularity that is not observed. Finally, recent experiments demonstrate that foam collapse takes much longer than the time available for the formation of the North Mono obsidian pyroclasts. Martel and Iacono-Marziano (2015) decompressed hydrous rhyolite at magmatic temperatures and pressures, causing their samples to vesiculate, and then eventually collapse in the manner proposed by Eichelberger et al. (1986). Their findings imply that at least 10^5 hours are required for foam collapse at the lowest melt viscosity that we expect during formation of the obsidian pyroclasts [$\eta \approx 10^6$ Pa s for 2.2 wt.% H_2O at T_m, using the method of Hess and Dingwell (1996)]. More viscous samples would take even longer. This is clearly inconsistent with both the time above T_g inferred from the heterogeneities of H_2O within the pyroclasts (Watkins et al., in press), and the wide gap in vesicularities between pumice and obsidian (Fig. 2). We conclude that some other process besides foam collapse led to the formation of the Mono Craters obsidian pyroclasts.

Some obsidian pyroclasts are composed of separate vesicular domains, and the contacts between them consist of xenocrysts and rock fragments (e.g., Figs. 7–8). This shows that some bands of ash-sized (and larger) xenocrysts became incorporated where pieces of obsidian sutured together. Some sutures remained as coherent bands through an obsidian pyroclast (Fig. 8a); other xenocryst bands are short, isolated trails only 10's to 100's of microns long. These disconnected bands most likely represent instances where obsidian fragments welded together more thoroughly. In some cases, there is evidence that these welded pyroclasts underwent further deformation and broke apart again, to leave small, isolated fragments of xenocrysts, which then welded together with other fragments. Each vesicular domain seen in Figure 7, for example, contains xenocryst bands orientated obliquely to the outer, xenocryst–lined sutures. This pyroclast thus records multiple cycles of fragmentation and suturing.

Distorted vesicles show textures that are also strongly suggestive of a fragmental origin. They are often organized into zones that separate regions of more-or-less vesicle-poor glass (Fig. 6a, b). These textures are consistent with partial sintering of fragments of obsidian and ash-sized glass of various sizes. The jagged and contorted shapes of the vesicles then result from the trapping of gas between the fragments. Indeed, the distorted vesicles seen in Figure 6c have multi-cuspate forms that are what one would expect if gas were trapped in the junctions between sintering glass fragments. The preservation of these distorted shapes requires that no significant relaxation of the trapped gas bubbles occurred; relaxation is discussed in detail later in Section 4.4.

This interpretation of the distorted vesicles is supported by their relationship to volatile heterogeneities and xenocryst bands. Watkins et al. (in press) found that the poorly vesicular regions in P2B–N (Fig. 6d) have different volatile contents than the bands of distorted vesicles that separate them. In addition, the glassy regions on either side of bands of distorted vesicles in P10–I (Fig. 6a) have different volatile contents. These domains are also separated by xenocryst bands and rock fragments. In general, vesicles that occur within xenocryst bands are most often distorted or stretched–distorted (Figs. 7, 8d), suggesting that xenocryst bands and distorted vesicles are linked, and both mark where ash and obsidian fragments sintered together.

4.3. Conceptual Model for the Formation of Obsidian Pyroclasts

Rust et al. (2004) proposed that some pyroclastic obsidians form through sintering of ash fragments. Here, we extend that model and argue that it is a general process that forms most, if not all, obsidian pyroclasts generated during the North Mono eruption. Xenocryst bands, which record cycles of fragmentation and sintering, are found in obsidian pyroclasts across the spectrum of measured volatile contents and in every tephra layer sampled, indicating that this process occurs over a wide range of depths in the conduit (Fig. 4), and at all stages of development of vesicular textures.

We argue that distorted vesicles are not relicts of collapsed magmatic bubbles, but are remnants of sintering, marking where ash fragments sintered together (Fig. 9). In this model, the spectrum of vesicle textures results from varying degrees of shearing and relaxation that act on starting populations of distorted vesicles formed by sintering. Both sintering and relaxation processes require time (see Section 4.4); consequently, the most likely location for these processes is at the conduit margin, where erupting material may be accreted and held for variable amounts of time, as proposed by Newman et al. (1988). After a packet of ash has begun to weld to form obsidian-like magma, it can be re–incorporated into the erupting mass and ejected to form obsidian pyroclasts with mainly distorted vesicles, or stretched–distorted vesicles if that packet is sheared shortly before (or while) it is re–incorporated (Fig. 9). Stalling for longer times at the margins of the conduit allows vesicles to relax, and thus re–incorporated pieces of this magma will produce obsidian pyroclasts with spherical to ellipsoid vesicles, depending on the degree of shear that acts on the packet (Fig. 9). The sequence of sintering, shearing, and relaxation can be repeated, resulting in pyroclasts with multiple domains of varying vesicular textures (Fig. 7, 8d).

Previous models suggest that obsidian forms in localized regions of fragmentation within a conduit that is otherwise filled with continuous magma. Rust et al. (2004) conclude that North Mono obsidian pyroclasts formed at conduit margins, where magma was brecciated by shear. Castro et al. (2014) conclude that obsidian lavas are produced through fragmentation and outgassing of vesicular magma along tuffisite veins. Although our data do not preclude these mechanisms, two lines of evidence support a model in which obsidian pyroclasts are formed in a conduit filled with fragmental material. First, the wide range in volatile contents indicates that obsidian formed over a great range of pressures (Table A.1) and hence depths (likely a few kilometers, depending on the density of the conduit-filling material), and was transported to the surface rapidly enough to preserve relatively steep gradients in volatile contents (Watkins et al., 2012; Watkins et al., in press). It is easier to imagine this happening in a conduit filled with an erupting gas-particle mixture than in one filled with continuous magma. Second, obsidian pyroclasts contain subdomains with different water contents. Although juxtaposition of clasts with different water contents can occur in tuffisite veins (Saubin et al., 2016), again it is easier to imagine this happening in a conduit filled with fast-moving fragmental material.

Our conceptualization requires that the environment at the conduit wall varies from depositional to erosional over time and space, suggesting that flow in the conduit is unsteady. It is possible that the sub–Plinian character of the eruption (Bursik, 1993) favors episodic cycling between deposition and erosion. Obsidian pyroclasts with higher volatile contents become less common up-section in the stratigraphy (Table A.1; Newman et al., 1988; Rust and Cashman, 2007; Barnes et al., 2014). It is possible that as the eruption waned (Sieh and Bursik, 1986), the main location for deposition and erosion of sintered material became shallower in the conduit.

Finally, we note that very similar vesicle textures are seen in obsidian pyroclasts erupted at Newberry Volcano (Rust and Cashman, 2007). Those pyroclasts also contain abundant veins of xenocrystic material. These features are compatible with our model, and we conclude that the Newberry Volcano samples could have formed by sintering of ash, suggesting that our model provides a general mechanism for generating obsidian pyroclasts.

4.4. Timescales and Conditions of Formation of Obsidian Pyroclasts

Our model postulates that the spectrum of vesicular textures results from varying degrees of shearing and relaxation of bubbles that were, originally, distorted gas pockets trapped between sintered fragments (Fig. 9). Both sintering and relaxation require that $T > T_g$, a condition that can exist for only a few hours at T_m across the range of H_2O contents (Watkins et al., in press). A first test of the model is to determine whether this allows sufficient time for bubble relaxation.

The characteristic relaxation time for a deformed bubble λ_b is given by equation 2. Surface tension is only weakly controlled by melt composition and T, and so for the limited range in H_2O contents of interest (Fig. 4) it is reasonable to assume that σ is constant, with a value of ~0.2 N m^{-1} (Walker and Mullins, 1981; Bagdassarov et al., 2000; Gardner and Ketcham, 2011; Gardner et al., 2013). Relaxation time therefore depends mainly on viscosity and bubble radius (Fig. 10). We note that the early stages of relaxation of a distorted bubble will proceed more rapidly because of the tighter radius of curvature, but for a bubble to become spherical, it must have an amount of time available for relaxation that is at least as long as the time calculated using equation 2 with the spherical bubble radius. Given the range in measured H_2O contents (Fig. 4), and allowing T to range from T_m to T_g, viscosity varies from ~10^6 to 10^{12} Pa s. Bubble radius varies over an approximate range of 1 to 100's of microns. Also shown in Figure 10 is the range in time allowed – bracketed at ca. 1–10 hours at T_m (Watkins et al., in press). This time is determined from modeling of diffusion of H_2O and CO_2, and diffusivity is a weaker function of temperature than is viscosity (Ni and Zhang, 2008); hence, the time allowed increases at $T < T_m$ as indicated by the shift to longer times at lower T. This analysis demonstrates that, at high H_2O content, there is ample time for bubbles to relax at T_m, and even near T_g there is still time for small bubbles to relax (Fig. 10a). At low H_2O contents, however, relaxation can only occur near T_m and only for relatively small bubbles (Fig. 10b).

A first–order conclusion, based on this analysis, is that distorted vesicles are more likely to be preserved in samples with lower H_2O content because the melt is more viscous and hence, bubbles relax more slowly. A logical corollary is that spherical vesicles should be more common in melts with higher H_2O content. We tested this hypothesis quantitatively using analysis of variance (ANOVA) of the H_2O and CO_2 contents of the pyroclasts, by dividing obsidian pyroclasts into three groups: distorted, spheroidal, and stretched. The "distorted" group includes samples with predominantly distorted or stretched-distorted vesicles; the "spheroidal" group includes samples with predominantly spherical, rounded ellipsoid, or sharp-tipped ellipsoid vesicles; and the "stretched" group includes samples with predominantly rounded ellipsoid, sharp-tipped ellipsoid, or stretched-distorted vesicles (thus it repeats some samples from each of the spheroidal and distorted categories). The rationale for these groupings is that distorted vesicles (whether stretched or not) indicate samples in which little bubble relaxation has occurred. Spheroidal vesicles, by contrast, represent samples in which bubbles have relaxed considerably. Samples with stretched vesicles should not differ from their non–stretched counterparts, except that they were sheared during, or shortly before, quench.

For H_2O concentrations, ANOVA indicates that the null hypothesis that samples in the spheroidal and distorted categories are drawn from the same distribution can be rejected at the 0.01% level (P-value = 0.000026). Hence, it is highly likely that samples in those two categories came from populations with different H_2O concentrations. By contrast, the null hypothesis that samples in the spheroidal and stretched categories are drawn from the same distribution cannot be rejected at the 1% level (P-value = 0.057). The same is true for the distorted and stretched categories (P-value = 0.040). The findings are the same for CO_2 concentrations, (P-values of 0.00011, 0.18, and 0.030, respectively, for the three null hypotheses). The volatile and vesicle shape data therefore support the hypothesis that spheroidal vesicles are more common in H_2O–rich (low viscosity) melts, whereas distorted vesicles are more common in H_2O–poor (high viscosity) melts (Fig. 4). The data in figure 14b of Rust and Cashman (2007) also support this broad correlation in North Mono obsidian pyroclasts.

More generally, our model postulates that distorted vesicles are gas pockets formed by sintering ash particles. Wadsworth et al. (2016) showed that the characteristic sintering timescale (λ_s) for randomly packed, monodisperse spherical particles of silicate melt is also given by equation 2, except with particle radius (L) replacing bubble radius r (i.e., $\lambda_S = \frac{\eta L}{\sigma}$). We do not have a direct measure of L, but can approximate it from the number density of distorted vesicles, such that $L \approx \sqrt[3]{N_V^{-1}}$. N_V ranges from $10^{5.3}$ to $10^{8.1}$ cm^{-3}, thus $L \approx$ 20–170 μm. Using the same values for surface tension and viscosity as above, and reading the vertical axis in Fig. 10 as particle radius, we find that there is ample time at high H_2O contents to sinter ash together across almost the entire range of temperature (Fig. 10a). At low H_2O contents, however, sintering is only likely for small ash sizes (Fig. 10b). We note that the sintering timescale presented is likely a maximum, because it assumes no shear or compression, both of which accelerate sintering (Rahaman et al, 1986; Rahaman and De Jonghe, 1990). Regardless, our analysis shows that, to first order, ash sintering can happen over the range of conditions of interest (time, magma temperature, and water content) of the eruption (Fig. 10).

Wadsworth et al. (2016) found that sintering monodisperse particles results in a final vesicularity of ~3 vol.%, whilst obsidian pyroclasts from the North Mono tephra typically have vesicularities of <1 vol.% (Table 1). It is likely that the initial population of ash particles is polydisperse, which allows sintering to proceed to lower vesicularities (Wadsworth et al., 2016). In addition, resorption of volatiles from vesicles into the melt, as a result of either cooling (McIntosh et al., 2014) or increased pressure (Watkins et al., 2012), would also lower vesicularity.

Our calculations indicate that sintering is favored for ash–sized particles (Fig. 10). This may explain why sintering of large pumice clasts is uncommon (Fig. 3f), even in an eruption that is generating abundant obsidian pyroclasts. Sintering may even require ash to act as the 'glue' that facilitates assembling larger clasts that are composed of smaller domains (e.g., Figs. 7, 8c, 8d). Xenolithic material often lines sutures between sub–domains, supporting this hypothesis. The lack of sutured pumice clasts may reflect a lower likelihood of trapping larger clasts at the conduit wall, because they presumably move with greater momentum and they typically make up a smaller proportion of the erupting mixture (e.g., Carey and Sigurdsson, 1982; Alfano et al., 2016).

4.5. Implications for Magmatic Degassing

The formation of obsidian pyroclasts by sintering of ash implies that the vesicles within them, and associated dissolved volatiles, reflect not only the degassing trends of bubbly magma but also the composition of gas trapped between particles. That volatile record can then be modified by internal diffusive re-equilibration (Watkins et al., in press) and distorted by break–up and re–sintering of disparate fragments (e.g., Fig. 8a). Variations in H_2O and CO_2 contents thus do not reflect either exclusively closed– or exclusively open–system trends (Newman et al., 1988).

Dissolved H_2O and CO_2 contents in obsidian pyroclasts are controlled by their solubilities, which are, in turn, controlled largely by pressure (Blank et al., 1993; Holtz et al., 1995; Liu et al., 2005). Accordingly, local volatile concentrations reflect pressures of formation, and suggest that obsidian pyroclasts formed at pressures ranging from ~3 to 43 MPa (Fig. 4). Additionally, in our model, dissolved H_2O and CO_2 contents reflect the composition of trapped gas. Volatile contents in each obsidian pyroclast indicate that the trapped gas composition, calculated using the model of Liu et al. (2005), ranges from 65 to 96 mol.% H_2O (Fig. 4). Gas composition does not vary systematically with inferred formation pressure; instead, its composition is roughly constant at 87±6 mol.% H_2O, despite the wide range in pressure, and regardless of vesicle type. Obsidian pyroclasts with mainly spherical bubbles record a gas of 87±5 mol.% H_2O, and those with distorted vesicles record a gas of 85±7 mol.% H_2O.

Our model generally supports the idea that the gas trapped in obsidian pyroclasts – and therefore the gas in the conduit – was buffered at a roughly constant composition (Rust et al., 2004). If it were not buffered, then it should have become progressively richer in H_2O from continued degassing of the ash (i.e., open–system degassing). In that case, gas trapped at shallow levels (low pressures) would be richer in H_2O, and the outcome would be that those obsidian pyroclasts with mainly distorted vesicles would contain a higher ratio of H_2O to CO_2 than those with mainly spherical vesicles, which is not what is seen (Fig. 9).

5. Conclusions

Obsidian pyroclasts from the ca. 1325–1350 C.E. eruption of North Mono tephra provide a window into processes that occurred in the conduit during the eruption. Detailed analysis of the vesicle textures show that a range of vesicle shapes exist, from highly distorted and multi-cuspate to spherical; vesicles also show variable degrees of shearing. Based on the inferred thermal-temporal environment in which the clasts formed, we show that vesicles of all types can be generated by relaxation and shearing of a starting population of distorted vesicles. We conclude that highly distorted vesicles represent the remnants of the interstitial spaces between sintered fragments of ash, and that all obsidian pyroclasts analyzed formed by sintering and relaxation of ash fragments. We also find that obsidian pyroclasts formed through repeated fragmentation and welding over a wide range of pressures (~3-43 MPa) – and hence a wide range of depths – within the conduit. We conclude that the conduit environment provides multiple opportunities for fragmented magma to stall, weld, and re-fragment, on its way to the surface. By contrast, we are able to eliminate the possibility that the obsidian pyroclasts formed through collapse of a permeable magma foam. The occurrence of similar vesicle textures and xenolithic material in obsidian pyroclasts in other eruptions (Rust and Cashman,

2007) suggests that ash sintering along conduit walls may be a general mechanism for generating obsidian pyroclasts.

Acknowledgements

The authors gratefully acknowledge B. Andrews, R. Zinke, and M. Manga for help in the field and helpful discussions; F. Wadsworth for discussions on sintering processes and obsidian formation; F. Worrall for assistance with statistical analysis; and T. Clow and J. Mariano for collection and analysis of HRXCT data. The authors also wish to Drs. Alison Rust and Yan Lavallée for their insightful reviews of this manuscript. The work was supported by NSF EAR–1348050 to JEG, NERC NE/N002954/1 to EWL, and NSF-EAR 1249404 to JMW. Funding for HRXCT scanning was provided in part by NSF grant EAR-1258878 to R. Ketcham, T. Rowe, and W. Carlson. JEG wishes to thank the Institute for Advanced Studies, Durham University, for their support and hospitality during preparation of this manuscript.

References

Alfano, F., Bonadonna, C., Watt, S., Connor, C., Volentik, A., and Pyle, D.M., 2016. Reconstruction of total grain size distribution of the climactic phase of a long-lasting eruption: the example of the 2008–2013 Chaitén eruption. Bull. Volcanol. 78, 46.

Bagdassarov, N., Dorfman, A., Dingwell, D. B., 2000. Effect of alkalis, phosphorus, and water on the surface tension of haplogranite melt. Am. Mineral. 85, 33-40.

Barnes, J.D., Prather, T.J., Cisneros, M., Befus, K., Gardner, J.E., and Larson, T.E., 2014. Stable chlorine isotope behavior during volcanic degassing of H_2O and CO_2 at Mono Craters, CA. Bull. Volcanol. 76, 805.

Befus, K.S., Gardner, J.E., and Zincke, R.W., 2013. Analyzing water contents in unexposed glass inclusions in quartz crystals. Am. Mineral. 97, 1898-1904.

Behrens, H., Tamic, N., and Holtz, F., 2004. Determination of the molar absorption coefficient for the infrared adsorption band of CO_2 in rhyolitic glasses. Am. Mineral. 89, 301–306.

Blank, J.G., Stolper, E.M., and Carroll, M.R., 1993. Solubilities of carbon dioxide and water in rhyolitic melt at 850 °C and 750 bars. Earth Planet. Sci. Lett. 119, 27–36.

Bursik, M., 1993. Subplinian eruption mechanisms inferred from volatile and clast dispersal data. J. Volcanol. Geotherm. Res. 57, 57-70.

Carey, S., and Sigurdsson, H., 1982. Influence of particle aggregation on deposition of distal tephra from the May 18, 1980, eruption of Mount St. Helens volcano. J. Geophys. Res. 87, 7061-7072.

Castro, J.M., Cordonnier, B., Tuffen, H., Tobin, M.J., Puskar, L., Martin, M.C., (2012) The role of melt-fracture degassing in defusing explosive rhyolite eruptions at Volcán Chaitén. Earth Planet Sci Lett 333-334, 63-69.

Castro, J. M., Bindeman, I. N., Tuffen, H., and Schipper, C. I., 2014. Explosive origin of silicic lava: textural and δD–H_2O evidence for pyroclastic degassing during rhyolite effusion. Earth Planet. Sci. Lett. 405, 52-61.

Eichelberger, J.C., and Westrich, H.R., 1981. Magmatic volatiles in explosive rhyolitic eruptions. Geophy. Res. Lett 8, 757–760.

Eichelberger, J.C., Carrigan, C.R., Westrich, H.R., and Price, R.H., 1986. Non-explosive silicic volcanism. Nature 323, 598–602.

Gardner, J.E., and R.A. Ketcham, 2011. Bubble nucleation in rhyolite and dacite melts: Temperature dependence of surface tension. Contrib. Mineral. Petrol. 162, 929-943.

Gardner, J.E., Ketcham, R.A., and Moore, G., 2013. The dynamics of bubble nucleation in hydrous mafic magmas. J. Volcanol. Geortherm. Res. 267, 68-74.

Gardner, J.E., R.M.E. Thomas, C. Jaupart, and S. Tait, 1996. Fragmentation of magma during volcanic plinian eruptions. Bull. Volcanol., 58, 144-162.

Ghiorso, M.S., and Evans, B.W., 2008. Thermodynamics of rhombohedral oxide solid solutions and a revision of the Fe-Ti two-oxide geothermometer and oxygen-barometer. Am. J. Sci. 308, 957-1039.

Gonnermann, H., and Manga, M., 2003. Explosive volcanism may not be an inevitable consequence of magma fragmentation. Nature 426, 432–435.

Gonnermann, H.M., and Manga, M., 2005. Nonequilibrium magma degassing: Results from modeling of the ca. 1340 A.D. eruption of Mono Craters, California. Earth Planet. Sci. Lett. 238, 1–16.

Gottsmann, J., Giordano, D., and Dingwell, D.B., 2002. Predicting shear viscosity during volcanic processes at the glass transition: a calorimetric calibration. Earth Planet. Sci. Lett. 198, 417–427.

Hess, K.–U., and Dingwell, D.B., 1996. Viscosities of hydrous leucogranitic melts: A non–Arrhenian model. Am. Mineral. 81, 1297–1300.

Holtz, F., Behrens, H., Dingwell, D.B., and Johannes, W., 1995. H2O solubility in haplogranitic melts: compositional, pressure, and temperature dependence. Am. Mineral. 80, 94–108.

Jaupart, C., and Allegre, C.J., 1991. Gas content, eruption rate and instabilities of eruption regime in silicic volcanoes. Earth Planet. Sci. Lett. 102, 413–429.

Kelleher, P.C., and Cameron, K.L., 1990. The geochemistry of the Mono Craters–Mono Lake Islands volcanic complex, Eastern California. J. Geophys. Res. 95, 17643–17659.

Ketcham, R.A., 2005. Computational methods for quantitative analysis of three-dimensional features in geological specimens. Geosphere 1, 32-41.

Kolzenburg, S., Heap, M.J., Lavallée, Y., Russell, J.K., Meredith, P.G., and Dingwell, D.B. (2012) Strength and permeability recovery of tuffisite-bearing andesite. Solid Earth 3, 191-198.

Llewellin, E.W., and Manga, M., 2005. Bubble suspension rheology and implications for conduit flow. J. Volcanol. Geotherm. Res. 143, 205–217.

Liu, Y., Zhang, Y., and Behrens, H., 2005. Solubility of H_2O in rhyolitic melts at low pressure and a new empirical model for mixed H_2O-CO_2 solubility in rhyolitic melts. J. Volcanol. Geotherm. Res. 143, 219-235.

Martel, C., and Iacono–Marziano, G., 2015. Timescales of bubble coalescence, outgassing, and foam collapse in decompressed rhyolitic melts. Earth Planet. Sci. Lett. 412, 173–185.

McIntosh, I.M., Llewellin, E.W., Humphreys, M.C.S., Nichols, A.R.L., Burgisser, A., Schipper, C.I., and Larsen, J.F., 2014. Distribution of dissolved water in magmatic glass records growth and resorption of bubbles. Earth Planet. Sci. Lett. 401, 1-11.

Newman, S., Epstein, S., and Stolper, E., 1988. Water, carbon dioxide and hydrogen isotopes in glasses from the ca. 1340 A.D. eruption of the Mono Craters, California: Constraints on degassing phenomena and initial volatile content. J. Volcanol. Geotherm. Res. 35, 75–96.

Ni, H., and Zhang, Y., 2008. H_2O diffusion models in rhyolitic melt with new high pressure data. Chem. Geol. 250, 68–78.

Nogauchi, S., Toramaru, A., and Nakada, S. (2008) Groundmass crystallization in dacite dykes taken in Unzen Scientific Drilling Project (USDP-4). J. Volcanol. Geotherm. Res., 175, 71-81.

Ochs, F.A., III, and Lange, R.A., 1999. The density of hydrous magmatic liquids. Science 283, 1314–1317.

Rahaman, M.N., Jonghe, L.C., and Brook, R.J., 1986. Effect of shear stress on sintering. J. Am. Cer. Soc. 69, 53-58.

Rahaman, M.N., and De Jonghe, L.C., 1990. Sintering of spherical glass powder under a uniaxial stress. J. Am. Cer. Soc. 73, 707-712.

Rust, A.C., and Manga, M., 2002. Bubble shapes and orientations in low Re simple shear flow. J. Coll. Interf. Sci. 249, 476–480.

Rust, A.C., and Cashman, K.V., 2007. Multiple origins of obsidian pyroclasts and implications for changes in the dynamics of the 1300 B.P. eruption of Newberry Volcano, USA. Bull. Volcanol. 69, 825–845.

Rust, A.C., Cashman, K.V., and Wallace, P.J., 2004. Magma degassing buffered by vapor flow through brecciated conduit margins. Geology 32, 349–352.

Saubin, E., Tuffen, H., Gurioli, L., Owen, J., Castro, J. M., Berlo, K., McGowan, E., Schipper, C.I., and Wehbe, K. (2016) Conduit Dynamics in Transitional Rhyolitic Activity Recorded by Tuffisite Vein Textures from the 2008–2009 Chaitén Eruption. Front. Earth Sci. 4:59, doi: 10.3389/feat.2016.00059.

Sieh, K, and Bursik, M., 1986. Most recent eruption of the Mono Craters, eastern central California. J. Geophys. Res. 91, 12539–12571.

Stasiuk, M.V., Barclay, J., Carroll, M.R., Jaupart, C., Ratté, J.C., Sparks, R.S.J., (1996) Degassing during magma ascent in the Mule Creek vent (USA). Bull. Volcanol., 58, 117-130.

Taylor, B.E., Eichelberger, J.C., and Westrich, H.R., 1983. Hydrogen isotopic evidence of rhyolitic magma degassing during shallow intrusion and eruption. Nature 306, 541–545.

Taylor, G.I., 1934. The formation of emulsions in definable fields of flow. Proc. Roy. Soc. Lond A 146, 501–523.

Tuffen, H., Dingwell, D.R., and Pinkerton, H. (2003) Repeated fracture and healing of silicic magma generate flow banding and earthquakes? Geology, 31, 1089-1092.

Wadsworth, F.B., Vasseur. J., von Aulock, F.W., Hess, K.U., Scheu, B., Lavallée, Y., and Dingwell, D.B., 2014. Nonisothermal viscous sintering of volcanic ash. J. Geophys. Res. 119, 8792–8804.

Wadsworth, F.B., Vasseur, J., Llewellin, E.W., Schauroth, J., Dobson, K.J., Scheu, B., and Dingwell, D.B., 2016. Sintering of viscous droplets under surface tension. Proc. Roy. Soc. A. 472:20150780.

Walker, D., and Mullins, Jr. O., 1981. Surface tension of natural silicate melts from 1200°-1500° C and implications for melt structure. Contrib. Mineral. Petrol 76, 455-462.

Watkins, J.M., Manga, M., and DePaolo, D.J., 2012. Bubble geobarometry: A record of pressure changes, degassing, and regassing at Mono Craters, California. Geology 40, 699-702.

Watkins, J.M., Gardner, J.E., and Befus, K.S. (in press) Non-equilibrium degassing, regassing, and vapor fluxing in magmatic feeder systems. Geology.

Westrich, H.R., and Eichelberger, J.C., 1994. Gas transport and bubble collapse in rhyolitic magma: an experimental approach. Bull. Volcanol. 56, 447–458.

Zhang, Y., Belcher, R., Ihinger, P.D., Wang, L., Xu, Z., and Newman, S., 1997. New calibration of infrared measurement of dissolved water in rhyolitic glasses. Geochim. Cosmochim. Acta 61, 3089-3100.

FIGURE CAPTIONS

Figure 1: Schematic stratigraphic sections for pits A and B, both of which were ~1.5–1.75 m in thickness. Pumice fragments and obsidian pyroclasts were collected from layers labeled “P” in the two pits. Pit A is the same as that in Barnes et al. (2012). Inset map shows the location of the two pits, relative to the positions of the obsidian domes and the cumulative tephra isopachs (in mm) for the ca. 1325–1350 C.E. Mono Craters eruption (modified from Newman et al., 1988).

Figure 2: Vesicularity distributions of pumice lapilli (open bars) and obsidian pyroclasts (solid bars). Tephra layer names mark the median pumice vesicularities. Although only 23 obsidian pyroclasts were measured, these are representative of the range of textures seen. P2B–24 is the one pumice lapilli that consists of smaller vesicular fragments sutured together with crystal–rich ash (See Fig. **3f**).

Figure 3: Slices from HRXCT scans of Mono Craters Pumice (white scale bar in each image is 1mm long). **a)** P10B–30, vesicularity = 74 vol.%. Note the relatively large range in vesicle sizes; **b)** P10B–41, vesicularity = 55 vol.%. Vesicle sizes are generally smaller than in more vesicular samples (compare to **a**); **c)** P6B–54, vesicularity = 52 vol.%. Note that this pumice has a denser microvesicular core (marked by arrow) that resembles less vesicular samples (see **d**); **d)** P2B–17, vesicularity = 44 vol.%. Vesicle sizes are significantly smaller than those in more vesicular samples; **e)** P6B–33, vesicularity = 41 vol.%. This pumice consists of highly

stretched vesicles, that appear to occur in bands that differ in the degree of stretching; **f)** P2B–24, vesicularity = 38 vol.%. this pumice consists of many smaller vesicular fragments sutured together with crystal-rich ash; some vesicular fragments are outlined to aid the reader. The ash also contains rock fragments (two of which are indicated by arrows).

Figure 4: H_2O–CO_2 concentrations in obsidian pyroclasts, with symbols indicating predominant vesicle type in the obsidian (see legend). The average error associated with the analyses is shown. Equilibrium fluid pressures (gray lines, in MPa) and fluid compositions (dotted lines, in mole fraction of H_2O) are shown, calculated from the model of Liu et al. (2005) and assuming T = 800°C.

Figure 5: Representative photomicrographs of spherical and ellipsoidal vesicle textures: **a)** spherical vesicles in P2–T (scale bar = 100 µm); **b)** clustered spherical vesicles in P4B–C (scale bar = 100 µm). Note that a few larger vesicles appear to have deformed the smaller surrounding vesicles; **c)** rounded ellipsoid vesicles in P2–N (scale bar = 300 µm); **d)** sharp-tipped ellipsoid vesicles in P2–S (scale bar = 500 µm).

Figure 6: Representative photomicrographs of distorted vesicle textures: **a)** and **b)** P10–I (note **b** is located within **a**; scale bar = 250 µm); **c)** P2B–D (scale bar = 100 µm); Representative photomicrographs of stretched–distorted vesicle textures: **d)** P2B–N (scale bar = 200 µm); **e)** P2B–B (scale bar = 200 µm); **f)** P6B-B (scale bar = 300 µm).

Figure 7: Representative photomicrograph of an obsidian pyroclast (P10-B) consisting of **a)** sub–domains of vesicle textures (outlined by curved dashed lines; scale bar = 1000 µm), many of which are divided by thin bands of xenocrysts and rock fragment, as shown in **b)**. Note that vesicles in the domains shown in **b** are orientated nearly 90° to each other and show differing degrees of stretching.

Figure 8: Representative photomicrograph of xenocryst bands in obsidian pyroclasts: **a)** Domains that differ in orientation of highly stretched–distorted vesicles in P4B–D, separated by a relatively sharp margin that contains numerous small xenocryst fragments (scale bar = 500 µm). Volatile contents of each region are shown. Note that vesicles are orientated differently and show different degrees of stretching in the two domains; **b)** plane polarized and **c)** cross polarized light images of a relatively coherent band of xenocrysts and glass with sharp margins in P4B–T (scale bar = 500 µm). Note small stretched-distorted vesicles in the pyroclast are orientated ~12° from parallel to the band. Small stringers of the band can be seen at its margin, which appear to be smeared off; those stringers are parallel to the orientation of the vesicles. Compare the high xenocryst abundance to the nearly holohyaline matrix; **d)** thin band of small xenocryst fragments in P4B–T (scale bar = 100 µm). This is a continuation of the same band in **a)**, but about 2 mm away.

Figure 9: Schematic model for the formation of obsidian pyroclasts. Ash collects and sinters along the margins of the volcanic conduit, forming distorted vesicles. Given time, vesicles relax to spherical under the stress of surface tension. Time allowed for

relaxation increases with increasing viscosity, which increases as temperature decreases from magmatic to the glass transition and as dissolved H_2O content decreases. Pyroclasts that contain spherical vesicles tend to be low viscosity (H_2O–rich), which is a statistically separate population from high viscosity (H_2O–poor) pyroclasts that contain distorted vesicles (ANOVA of H_2O contents based on *n* number of samples). Vesicles are stretched if shear is exerted on the vesicular magma. If exerted soon after sintering, then stretched–distorted vesicles result; if exerted late, then smooth, elongated vesicles result. H_2O contents of pyroclasts with sheared vesicles overlap with the other populations as expected from being those pyroclasts that experienced shear.

Figure 10: Time required for a bubble of radius *r* to relax or ash particle of size *L* to sinter as a function of temperature, for **a)** 2.2 wt.% H_2O and **b)** 0.49 wt.% H_2O; these values are the highest and lowest water contents measured in our samples. The gray band delimits the time available for these processes during the North Mono eruption, based on H_2O diffusion modeling of Watkins et al (in press). Dashed curves are where sintering and relaxation take longer than the time allowed by diffusion modeling. Surface tension (σ) equals 0.2 N m^{-1} for all times.

Figure

Click here to download Figure: Fig 1.pdf

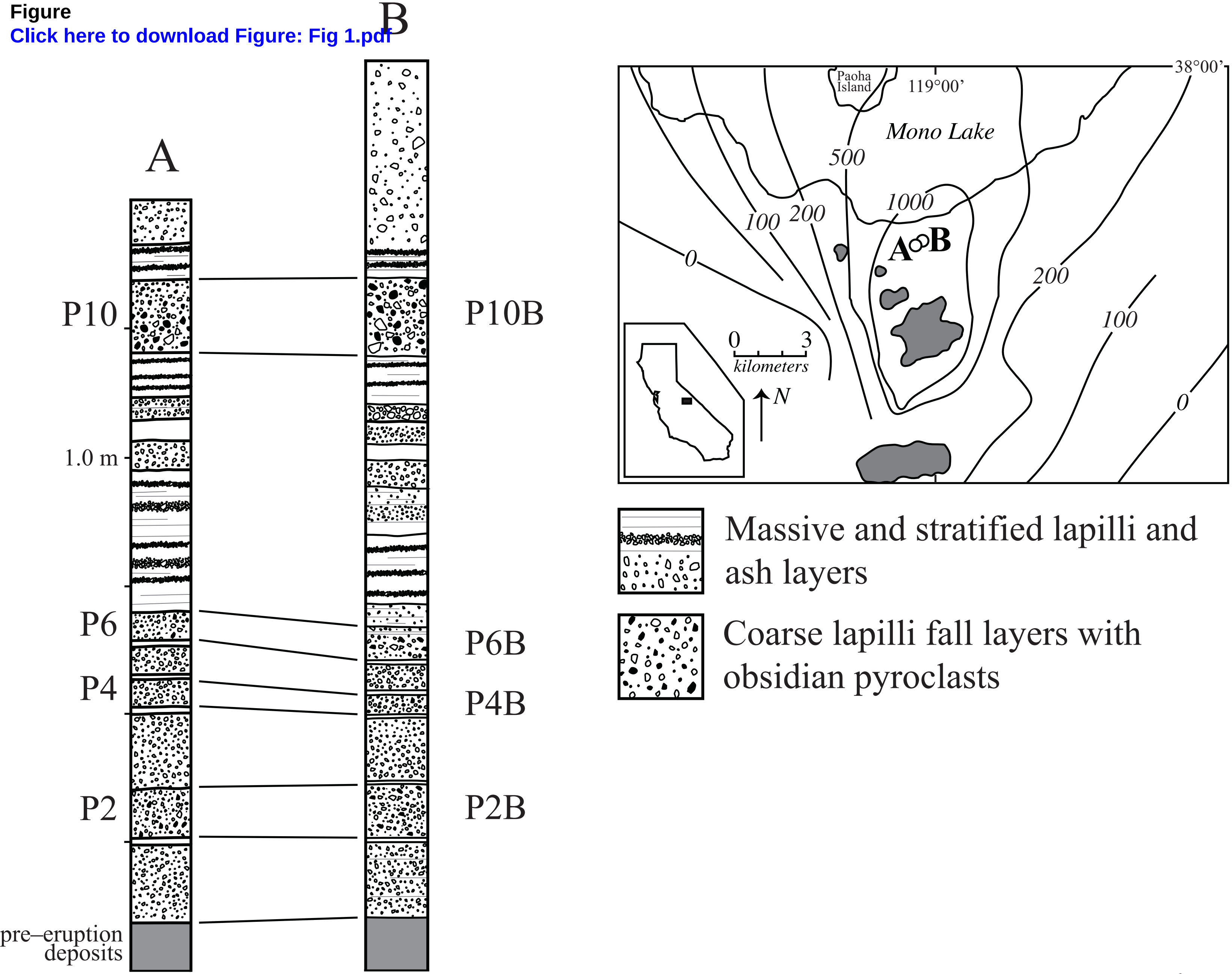

Figure 1

Figure
Click here to download Figure: Fig 2.pdf

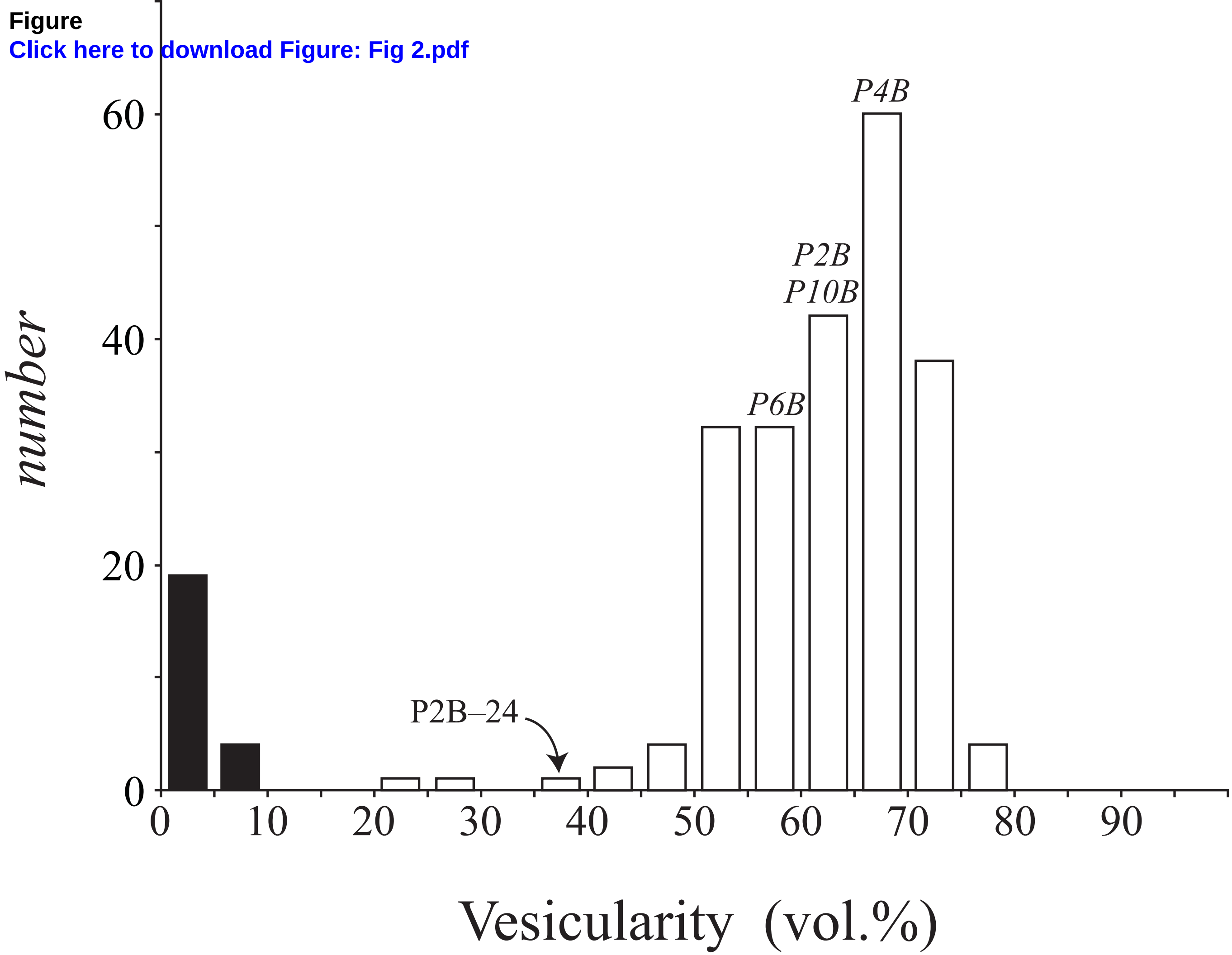

Figure 2

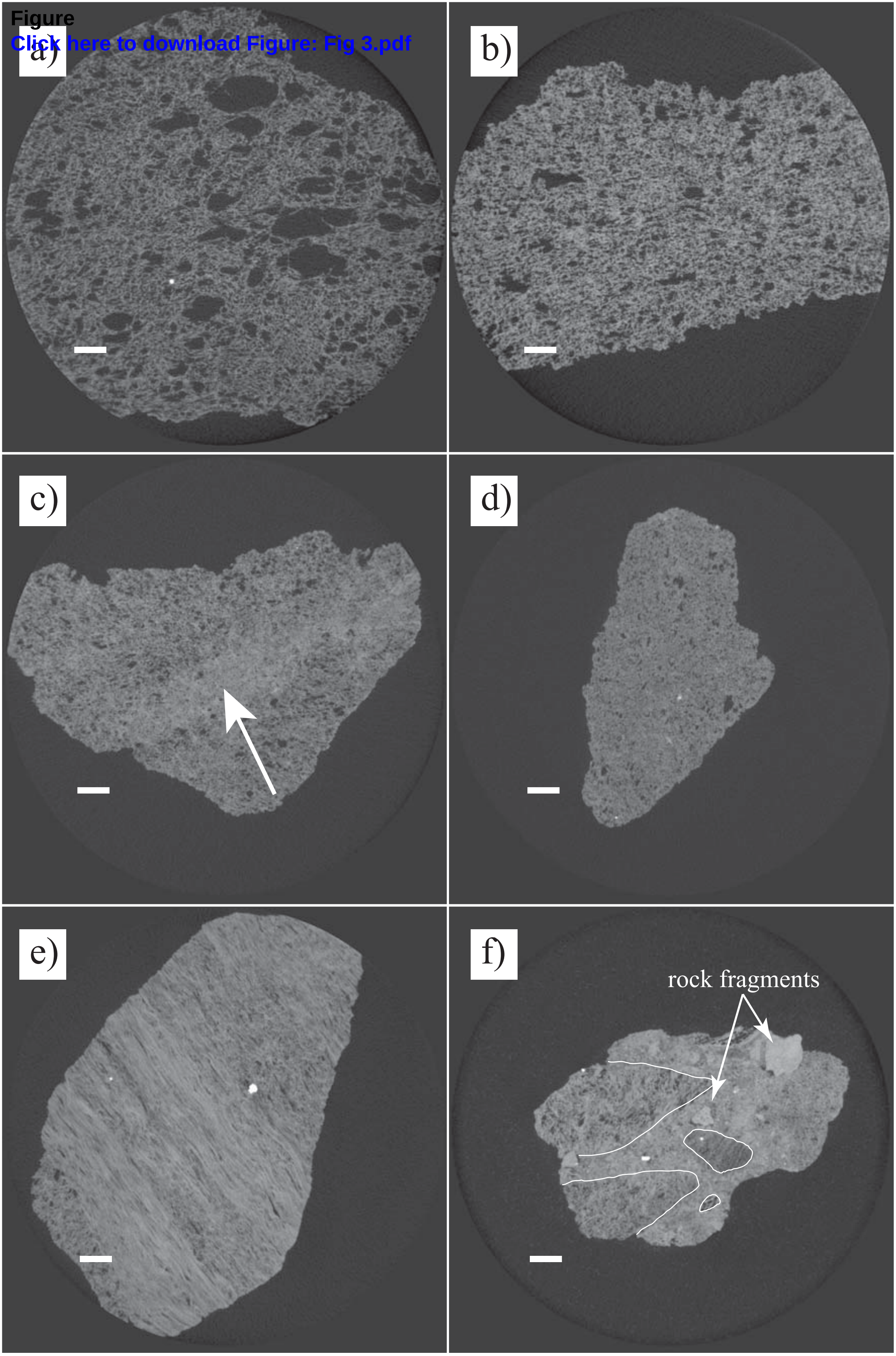

Figure 3

Figure

Click here to download Figure: Fig 4.pdf

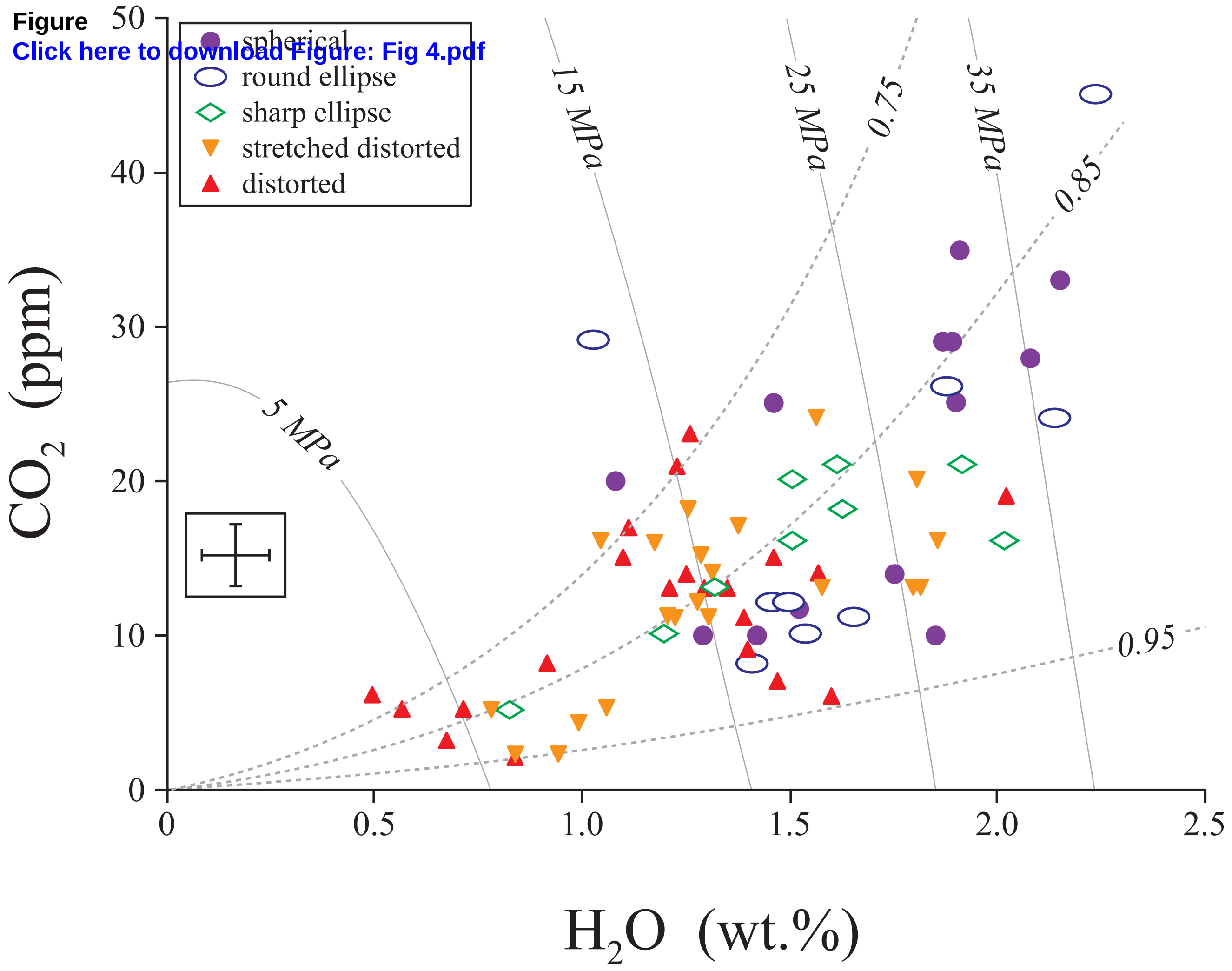

Figure 4

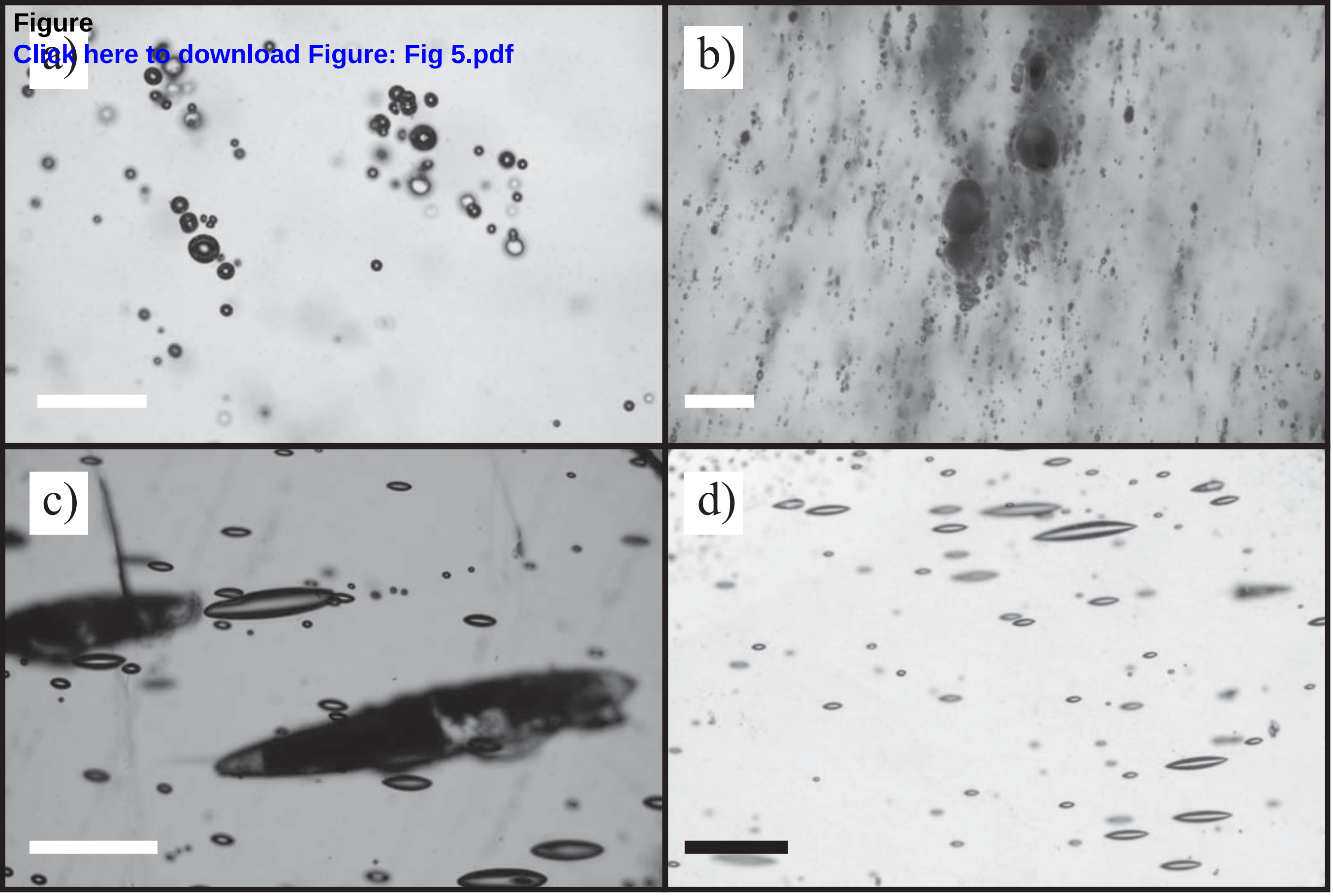

Figure 5

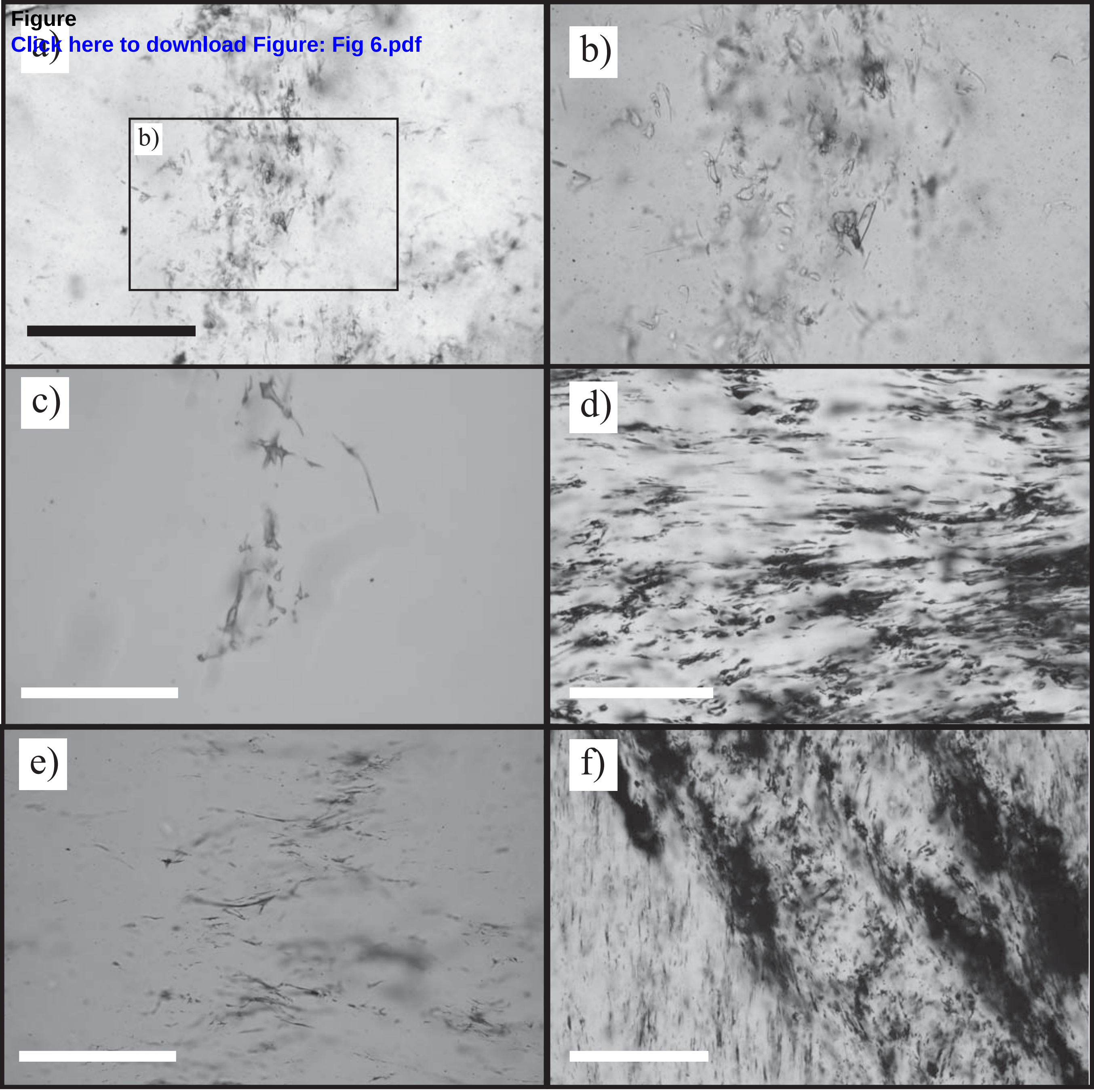

Figure 6

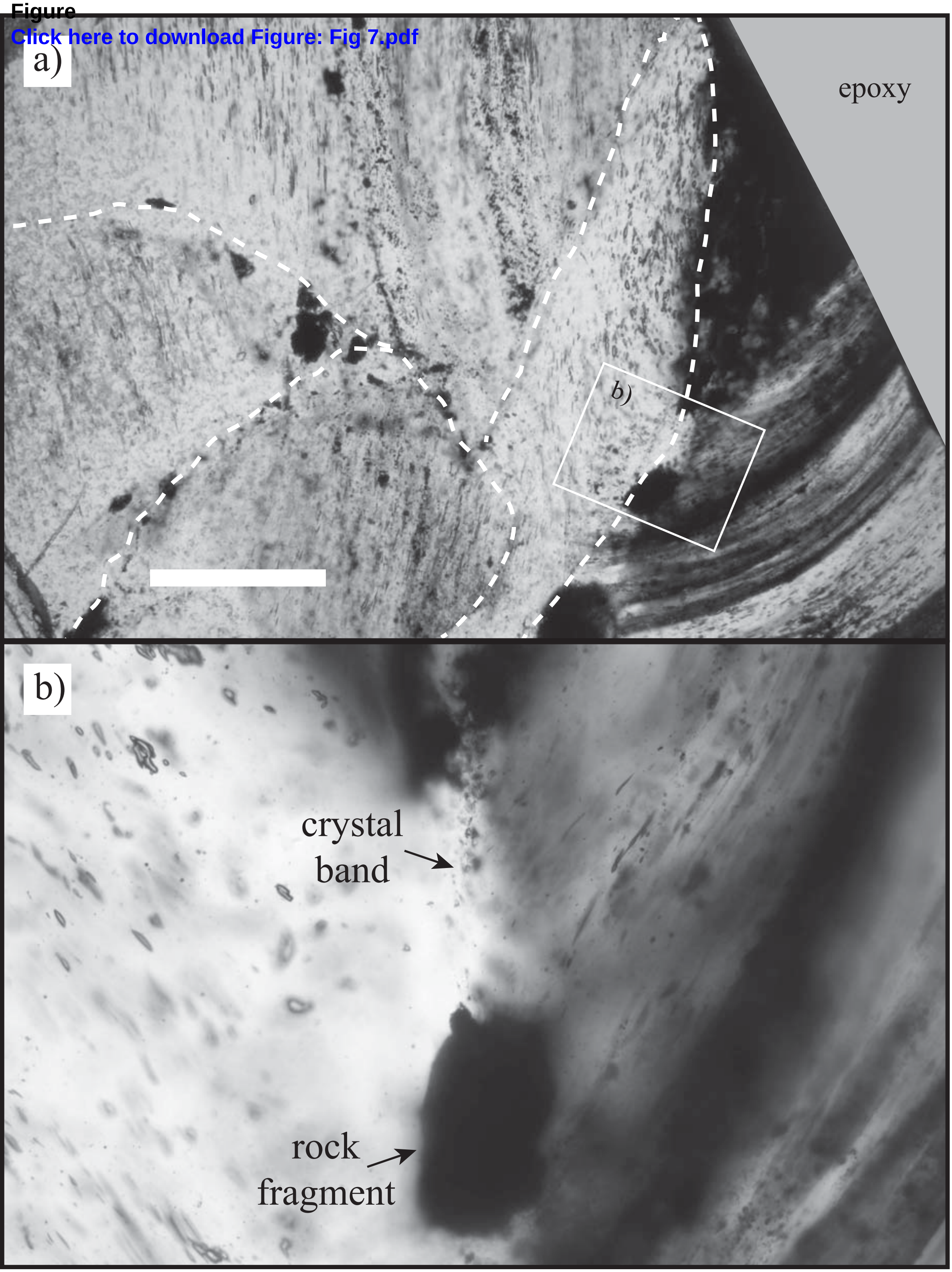

Figure 7

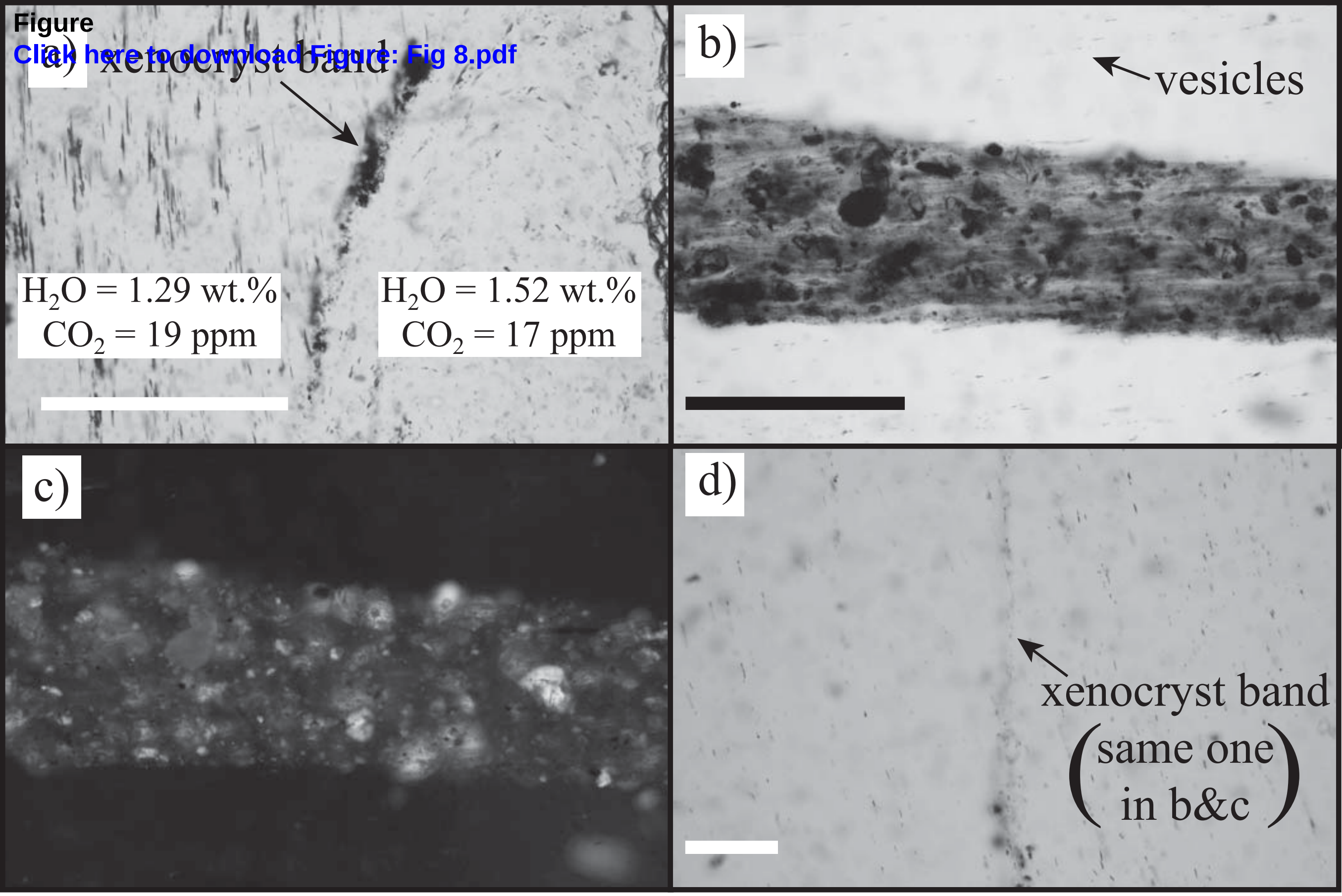
a) xenocryst band
H_2O = 1.29 wt.%
CO_2 = 19 ppm
H_2O = 1.52 wt.%
CO_2 = 17 ppm
b)
vesicles
c)
d)
xenocryst band
(same one in b&c)

Figure 8

Figure
Click here to download Figure: Fig 9.pdf

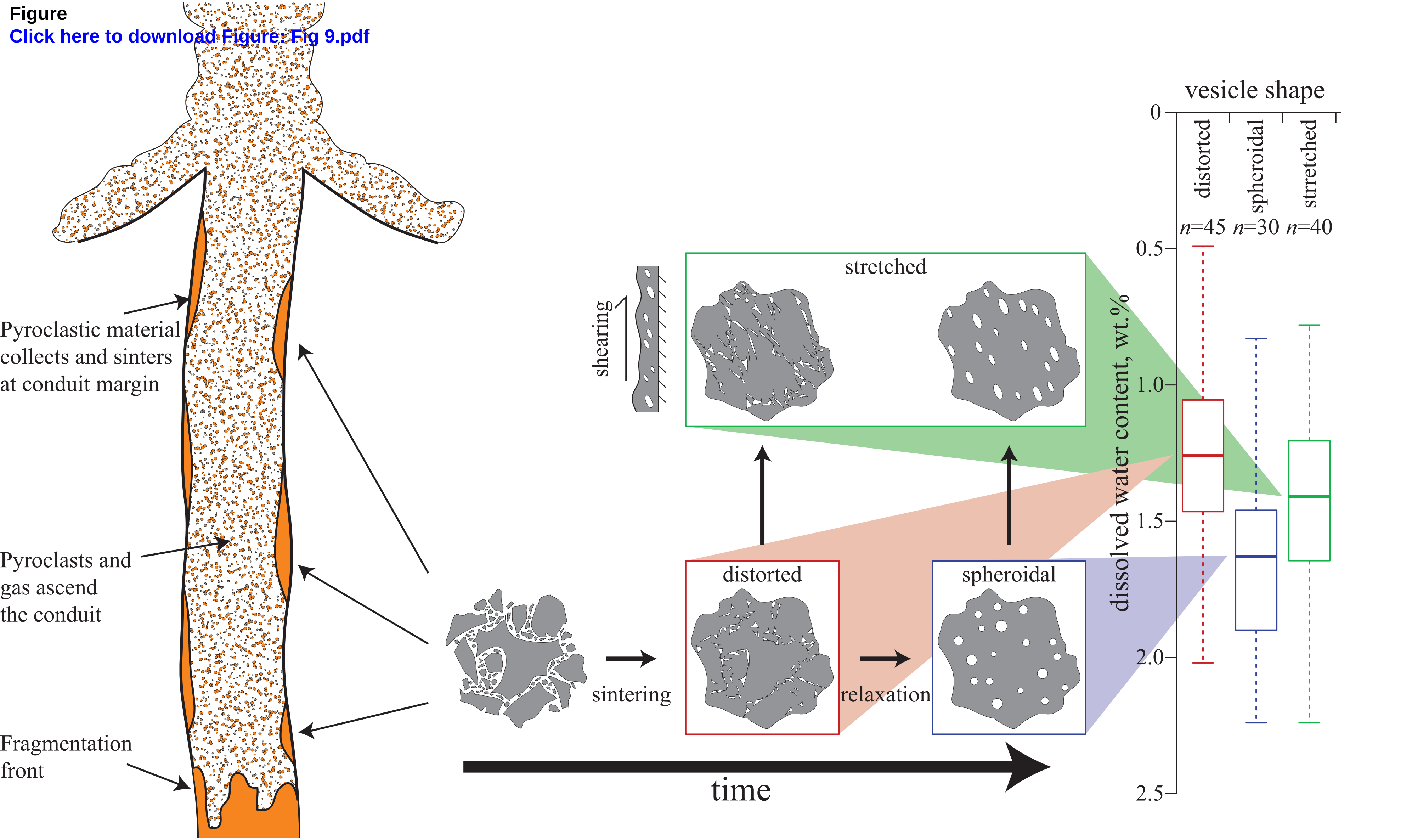

Figure 9

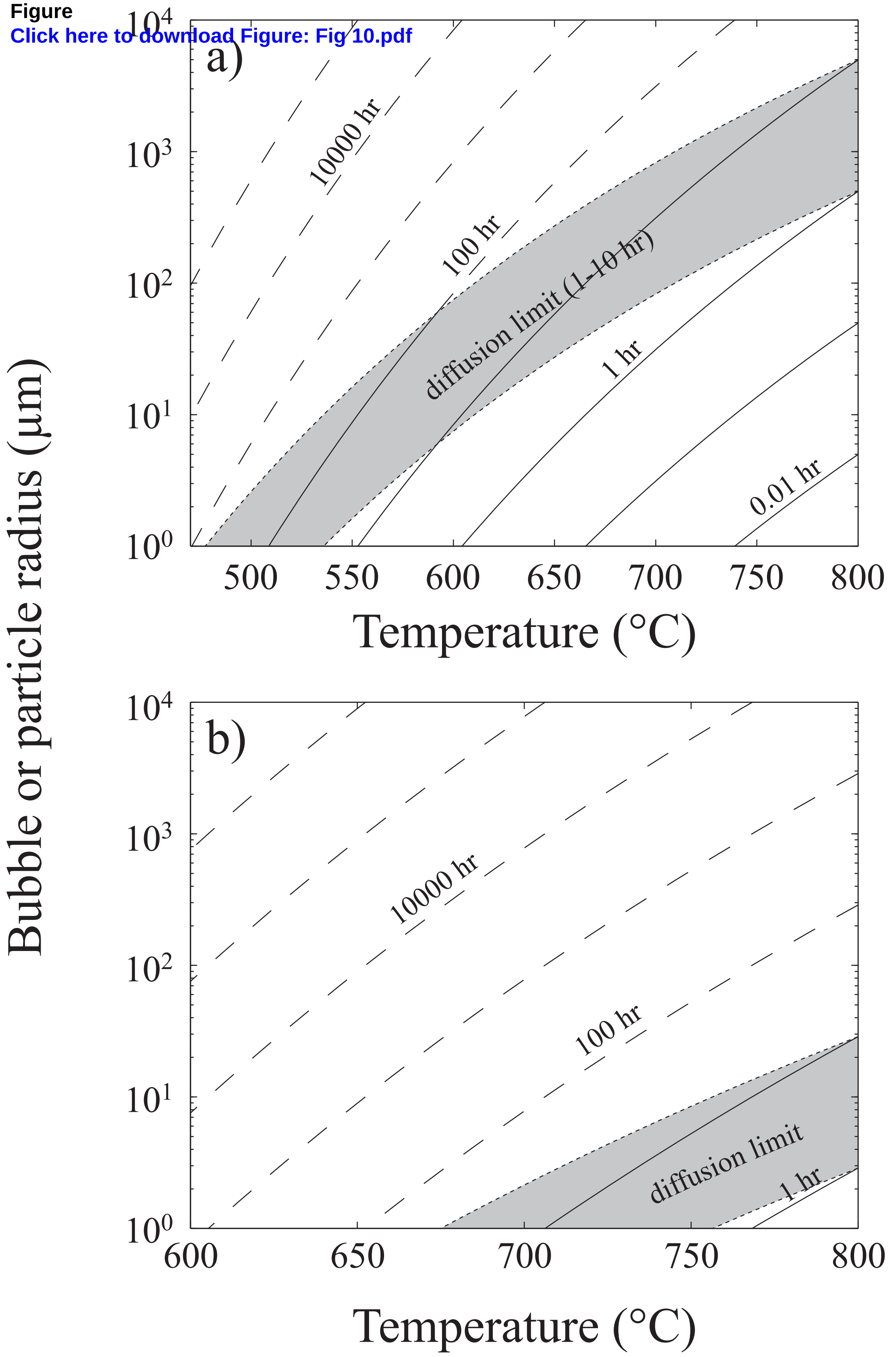
a)
10000 hr
100 hr
diffusion limit (1-10 hr)
1 hr
0.01 hr
Bubble or particle radius (μm)
Temperature (°C)
500
550
600
650
700
750
800
b)
10000 hr
100 hr
diffusion limit
1 hr
600
650
700
750
800

Figure 10